

# High pressure microreactor for minute amounts of catalyst on planar supports: A case study of CO<sub>2</sub> hydrogenation over Pd<sub>0.25</sub>Zn<sub>0.75</sub>O<sub>x</sub> nanoclusters



Imran Abbas <sup>a,\*</sup>, Filippo Romeggio <sup>b</sup>, Kacper Pilarczyk <sup>a,c</sup>, Simon Kuhn <sup>d</sup>, Christian Danvad Damsgaard <sup>b,e</sup>, Jakob Kibsgaard <sup>b</sup>, Peter Lievens <sup>a</sup>, Didier Grandjean <sup>a</sup>, Ewald Janssens <sup>a,\*</sup>

<sup>a</sup> Quantum Solid-State Physics, Department of Physics and Astronomy, KU Leuven, Celestijnenlaan 200D, 3001 Leuven, Belgium

<sup>b</sup> Department of Physics, Technical University of Denmark, 2800 Kongens Lyngby, Denmark

<sup>c</sup> Faculty of Physics and Applied Computer Science, AGH University of Science and Technology, al. A. Mickiewicza 30, 30-059 Kraków, Poland

<sup>d</sup> Department of Chemical Engineering, KU Leuven, Celestijnenlaan 200F, 3001 Leuven, Belgium

<sup>e</sup> National Centre for Nano Fabrication and Characterization, Technical University of Denmark, 2800 Kongens Lyngby, Denmark

## ARTICLE INFO

### Keywords:

High-pressure microreactor  
Cluster-based catalyst  
PdZnO  
CO<sub>2</sub> hydrogenation  
Reverse water–gas shift reaction

## ABSTRACT

High-pressure studies of well-defined catalysts, deposited on planar supports in ultra-high vacuum using physical methods, may bridge the gap between surface science and applied catalysis approaches in order to develop better catalysts for crucial reactions such as CO<sub>2</sub> hydrogenation. However, the chemical reactors necessary for such investigations, typically involving catalyst quantities down to a few hundred nanograms, are lacking.

We present the novel design and evaluation of a 50 μL rectangular microchannel reactor capable of testing small quantities of catalyst at pressures up to 40 bar and temperatures up to 240 °C. To evaluate the microreactor performance, Pd<sub>0.25</sub>Zn<sub>0.75</sub>O<sub>x</sub> nanoclusters soft-landed on SiO<sub>2</sub>-coated mica sheets using the cluster beam deposition technique, were tested for CO<sub>2</sub> hydrogenation via the reverse water–gas shift reaction through a series of kinetic experiments.

Experimental results, combined with computational fluid dynamics and mass transport analysis, demonstrate that the proposed microreactor setup allows for testing minute quantities of catalysts with very high sensitivity at industrially relevant temperatures and pressures. Although not restricted to a particular catalyst preparation method, the setup is an excellent platform for conducting catalytic tests on composition-controlled, mass-selected, gas-phase nanoparticles deposited on planar substrates, facilitating the determination of reliable structure–activity relationships and enabling a more rational design of catalysts.

## 1. Introduction

The urgent need to combat climate change has prompted an increasing focus on CO<sub>2</sub> utilization as a means to reduce greenhouse gas emissions and achieve a more sustainable future [1]. Among the various pathways for CO<sub>2</sub> utilization, thermochemical CO<sub>2</sub> conversion to fuels and valuable chemicals using a solid catalyst is promising. Heterogeneous catalysis offers immediate product separation and an industrially-proven technology to process upscaling and integration in the contemporary chemical industry [2]. Central to this endeavor is the search for efficient and stable catalysts that are selective towards one of the various

CO<sub>2</sub> hydrogenation products [3]. Rational design of highly active and selective catalysts necessitates a comprehensive understanding of the nature and structure of their active sites [4,5].

Current approaches for investigating these active sites can be broadly categorized into two groups namely (i) the surface science approach and (ii) the applied catalysis approach. The surface science approach involves the investigation of well-defined catalytic surfaces, traditionally in ultra-high vacuum conditions, to establish a relationship between the structure of the catalyst and its activity [6]. However, extrapolating these structure–activity relationships from ultra-high vacuum to industrial conditions remains challenging, as catalyst structure and behaviour can vary significantly with changes in pressure — a phenomenon

\* Corresponding authors.

E-mail addresses: [imran.abbas@kuleuven.be](mailto:imran.abbas@kuleuven.be) (I. Abbas), [ewald.janssens@kuleuven.be](mailto:ewald.janssens@kuleuven.be) (E. Janssens).

Nomenclature	
A	Pre-exponential factor
$A_r$	Area of catalytic surfaces ( $\text{m}^2$ )
$\text{AS}_{(\text{ads})}$	Surface species
$a_s$	$A_r$ to $V_r$ ratio ( $\text{m}^{-1}$ )
$\alpha$	Partial order of the reaction with respect to $\text{CO}_2$
$\beta$	Partial order of the reaction with respect to $\text{H}_2$
$C_j$	Concentration of species $j$ ( $\text{mol}/\text{m}^{-3}$ )
$d$	Diameter of the nanocluster (nm)
$D_j$	Diffusion coefficient of species $j$ ( $\text{m}^2 \text{s}^{-1}$ )
$Da$	Damköhler number
$Da_{II}$	Damköhler number II
$E_a$	Activation energy ( $\text{J mol}^{-1}$ )
eV	Electronvolt
$F_{\text{CO}_2}$	Molar flow rate of $\text{CO}_2$ ( $\text{mol s}^{-1}$ )
$h_{ML}$	Loading expressed in equivalent atomic monolayers (ML)
$\Phi_{ma}$	Mass flux of the nanoclusters ( $\text{ng cm}^{-2} \text{min}^{-1}$ )
$h$	Channel height ( $\mu\text{m}$ )
$k$	Reaction rate constant
$m$	Mass (kg)
$\mathbf{n}$	Normal vector to the surface with catalyst
$\Omega_D$	Collision integral
$\rho$	Density of the nanocluster ( $\text{kg m}^{-3}$ )
$p$	Pressure (Pa)
Pe	Peclet number
R	Gas constant (approx. $8.314 \text{ J mol}^{-1}\text{K}^{-1}$ )
$R^2$	R-squared value
$R_j$	Rate of production (or consumption) of species $j$ ( $\text{mol}/\text{m}^{-3}$ $\text{s}^{-1}$ )
$R_{ads,j}$	Rate of adsorption (or desorption) of species $j$ per unit $A_r$ , ( $\text{mol m}^{-2} \text{s}^{-1}$ )
$\sigma$	Characteristic length of the Lennard-Jones/Stockmayer potential (m)
T	Absolute temperature (K)
$\tau$	Mean residence time (s)
$t_D$	Maximal diffusion time (s)
$\mu$	Dynamic viscosity (Pa·s)
$\mathbf{u}$	Velocity field (m/s)
$v_0$	Volumetric flow rate at reaction conditions ( $\text{cm}^3 \text{s}^{-1}$ )
$V_r$	Volume of the reactor ( $\text{m}^3$ )
cat	Catalyst
CBD	Cluster Beam Deposition
EXAFS	Extended X-ray Absorption Fine Structure
EDX/EDS	Energy Dispersive X-Ray Spectroscopy
FT	Fourier Transform
FID	Flame Ionization Detector
GC	Gas Chromatograph
ICP	Inductive Coupled Plasma
ML	Equivalent atomic MonoLayer
QCM	Quartz Crystal Microbalance
RWGS	Reverse Water Gas Shift
SEM	Scanning Electron Microscopy
sccm	Standard cubic centimeter per minute
TCD	Thermal Conductivity Detector
TOF-MS	Time-of-Flight Mass Spectrometry
XAS	X-ray Absorption Spectroscopy
XANES	X-ray Absorption Near Edge Structure

commonly referred to as the “pressure gap” [7,8]. Additionally, the investigated surfaces may differ in size and morphology from those of the actual supported nanoparticles used in practical catalysts operating at industrial conditions, introducing another challenge known as the “material gap” [9,10].

In contrast, the applied catalysis approach addresses the material and pressure gaps by mimicking industrially relevant conditions to prepare and test catalysts, including the use of high-pressure laboratory reactors [11]. However, the inherent structural complexity of these (usually chemically prepared) heterogeneous catalysts complicates the characterization of the active sites, particularly under reaction conditions. This severely impedes the identification of reliable structure–activity relationships [12]. Additionally, dynamic changes in the catalyst as well as the impact of ligands and remnant impurities from the chemical synthesis route add to the uncertainty in the results [13]. These challenges have, for example, contributed to the lack of consensus on the nature of active sites in methanol synthesis catalysts studied for decades [14].

To address the pressure and material gaps while minimizing the structural complexity of heterogeneous catalysts, there is a need to prepare well-defined surfaces and nanoparticles that are free of impurities and ligands, and to test them under industrially relevant pressures and temperatures [15–19]. This can be achieved by combining the strengths of surface science and applied catalysis approaches. The preparation of catalyst nanoparticles with precisely tailored size, composition, and oxidation state is possible using gas aggregation cluster sources and the Cluster Beam Deposition (CBD) technique [20–24]. However, an inherent limitation of this synthesis technique to perform activity tests at industrially relevant conditions is that it produces small quantities of catalysts, typically ranging from 20 to 200 ng/min. These catalyst quantities are typically 3–4 orders of magnitude smaller than the mass loading required for activity tests in traditional

laboratory reactors. As a result, a specialized microreactor designed to handle these extremely small catalyst quantities on planar substrates is necessary to ensure sufficient contact time at lower feed gas flow rates, while minimizing product dilution. Additionally, the geometry of the reactor should be suitable for planar samples.

Some research groups have developed dedicated reactors for testing small quantities of catalysts deposited on planar supports. One notable example is a reactor microfabricated in a silicon chip for catalytic activity tests and surface kinetics. This reactor was employed for testing soft-landed mass-selected  $\text{AuTiO}_x$  nanoparticles for CO oxidation [25,26] and NiGa thin films for  $\text{CO}_2$  hydrogenation to methanol at pressures up to 1 bar [27]. Another reactor, designed for gas phase reactions using minimal catalyst quantities was used for the dehydrogenation of cyclohexene and  $\text{CO}_2$  hydrogenation at ambient pressures [28,29]. More recently, a microreactor was developed and employed for activity characterization of thin films (3 nm Pd) at 1 bar and 100 °C [30].

To the best of our knowledge, no microreactor has been reported to study ultrasmall quantities of catalysts on planar substrates at high pressures (10 bar or more). In response, we have designed a microreactor specifically tailored for testing planar substrates decorated with catalyst quantities down to a few hundred nanograms (or below 1 atomic monolayer) of catalyst at pressures up to 40 bar.

In this manuscript, we present a comprehensive case study of the microreactor’s performance, using  $\text{CO}_2$  hydrogenation to CO via the Reverse Water-Gas Shift (RWGS) reaction on  $\text{Pd}_{0.25}\text{Zn}_{0.75}\text{O}_x$  catalyst. While the RWGS reaction itself does not require high pressure, the reactions were performed at conditions relevant for industrial methanol synthesis, i.e., 40 bar and 200–250 °C. Additionally, CO produced at high pressure from  $\text{CO}_2$  and (renewable)  $\text{H}_2$  can serve as a valuable feedstock for several key industrial processes performed at high-pressure, e.g., methanol synthesis and the Fischer-Tropsch synthesis processes for fuel production [31,32].

Bimetallic PdZnO<sub>x</sub> nanoparticles are known to be efficient catalysts for several important reactions, including methanol steam reforming, CO oxidation, alcohol oxidation, and CO<sub>2</sub> hydrogenation [33–35]. Their ability to produce different CO<sub>2</sub> hydrogenation products depending on the catalyst composition and the type of support has been the subject of several studies. Pd/ZnO and PdZn-ZnO interfaces have been associated with methanol production [36,37]. Investigations involving various Pd:Zn ratios deposited on TiO<sub>2</sub> and CeO<sub>2</sub> revealed the presence of  $\beta$ -PdZn alloy in Zn-rich compositions, which has been highlighted for its role in CO<sub>2</sub> hydrogenation to methanol and CO via the RWGS reaction [38–41].

We prepared Pd<sub>0.25</sub>Zn<sub>0.75</sub>O<sub>x</sub> nanoclusters in ultra-high vacuum using a laser ablation gas aggregation cluster source [24] and soft-landed them onto mica sheets coated with nano-dispersed SiO<sub>2</sub>. These planar samples were investigated in the new microreactor in a 3H<sub>2</sub>:1CO<sub>2</sub> feed gas flowing at 0.5–4 sccm (0.08–0.32 sccm/ $\mu\text{g}_{\text{cat}}$ ). Activity results were fitted with a power-law model to extract the kinetic parameters of the reaction which were then used in reacting fluid dynamics simulations to validate the design of the microreactor. The results demonstrate that the reactivity of minute quantities of catalysts deposited on planar substrates can be accurately measured with high sensitivity and under industrially relevant conditions. This approach helps bridging the gap between surface science and applied catalysis approaches, facilitating the development of reliable structure–activity relationships, thereby enabling the rational design of highly efficient catalysts.

## 2. Experimental methods

### 2.1. Design and fabrication of microreactor

The microreactor consists of two precisely machined stainless steel plates. The bottom plate has a rectangular cavity of 50 × 18 × 0.22 mm<sup>3</sup>, tailored to accommodate a 150–200  $\mu\text{m}$  thick planar catalyst substrate decorated with nanoclusters. Positioned 2 mm away from each edge of the sample cavity on all sides, a 2.2 mm deep groove is carved, providing housing for a Kalrez O-ring (47.29 mm ID × 2.62 mm CS, FFKM 300B AED 90 ShA) to ensure a leak-tight seal. For thicker planar substrates, a similar bottom plate with a deeper cavity can be prepared.

The top plate was machined to craft a 1 mm wide rectangular fin with a height of 70  $\mu\text{m}$  that inserts into the sample cavity of the bottom plate, exerting uniform pressure on all edges of the planar catalyst substrate. This meticulous design ensures the creation of a reactor volume of around 50  $\mu\text{L}$  ( $\approx 48 \times 16 \times 0.07 \text{ mm}^3$ ) with a reproducible gap of 70  $\mu\text{m}$ .

between the top plate and the catalyst substrate when the two plates are securely tightened against each other using 10 screws. A K-type thermocouple, compression-fitted in the top plate, slightly presses the middle of the sample to accurately monitor its temperature. The entire microreactor is placed inside the constant temperature zone of a tube furnace, as schematically shown in Fig. 1.

Compression-type fittings for 1/32" capillaries are seamlessly integrated into the top plate to introduce the reaction gas mixture and allow the outflow of products. Low-flow mass flow controllers (Bronkhorst High-Tech B.V.) are employed to control the gas flow rates into the microreactor. The products leave the microreactor through a 130  $\mu\text{m}$  internal diameter stainless-steel capillary (Valco Instruments Co. Inc.) to reach a T-piece, where helium carrier gas can be introduced to accelerate the flow towards a backpressure regulator with a small dead volume (Equilibar® USA) and subsequently to the gas chromatograph (GC). The accelerated product flow rate lowers the response time of the GC to changes in the reaction conditions.

The products are analyzed using a customized GC (Thermo Fisher Scientific) which has small internal dead volume and requires only 150  $\mu\text{L}$  of sample to quantify up to 1 ppm of CO, methane, methanol, ethanol, ethylene, and dimethyl ether.

### 2.2. Substrate preparation

Planar substrates for the nanocluster deposition consist of inert mica sheets (Grade V-5, Structure Probe, Inc.) nanostructured by coating them with SiO<sub>2</sub> nanoparticles. 40  $\mu\text{L}$  of a 50 wt% SiO<sub>2</sub> nanoparticle dispersion (Thermo Fisher, Product No. 43109) was drop-casted onto a 50 × 18 × 0.15 mm<sup>3</sup> mica sheet and evenly spread using a doctor-blade technique, resulting in a 20  $\mu\text{m}$  coating composed of 20 nm SiO<sub>2</sub> nanoparticles. After air-drying, these substrates were used for nanocluster catalyst deposition and characterization, as schematically shown in Fig. 2.

### 2.3. Cluster-based catalyst deposition

The SiO<sub>2</sub>-coated mica substrates were decorated with Pd<sub>0.25</sub>Zn<sub>0.75</sub>O<sub>x</sub> nanoclusters produced in a laser ablation-based cluster source [42], operating in ultra-high vacuum conditions (base pressure 10<sup>-8</sup> mbar). As precursor material, a bimetallic PdZn alloy target (ACI alloys, 99.99 % purity) is installed in a liquid nitrogen-cooled source for nanocluster synthesis. The target is ablated by the 2nd harmonic of a pulsed Nd:YAG

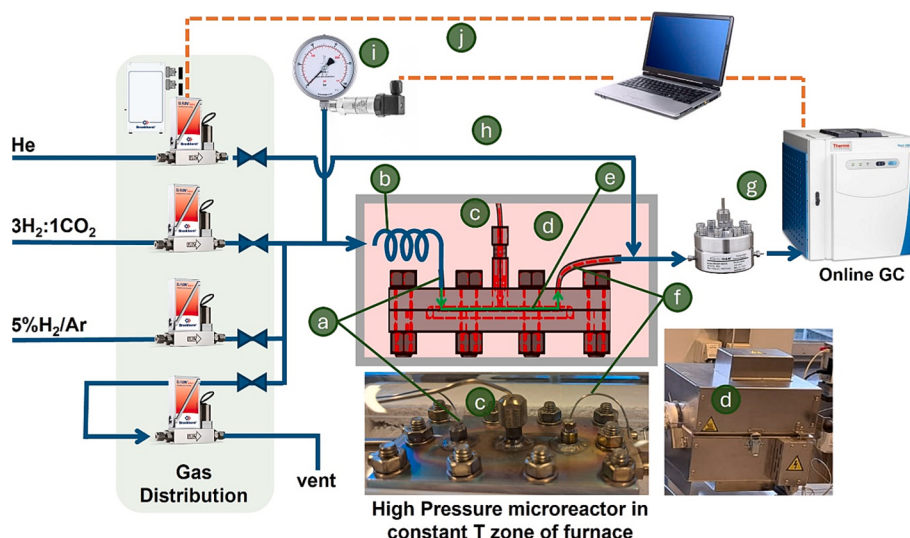


**Fig. 1.** Schematics of the experimental setup with the microreactor: (a) Inlet, (b) preheater, (c) thermocouple, (d) tube furnace housing the microreactor, (e) gas flow path through the microchannel, (f) outlet, (g) back pressure regulator, (h) gas flow capillaries (blue lines), (i) pressure gauges, (j) data communication (orange lines). (For interpretation of the references to colour in this figure legend, the reader is referred to the web version of this article.)

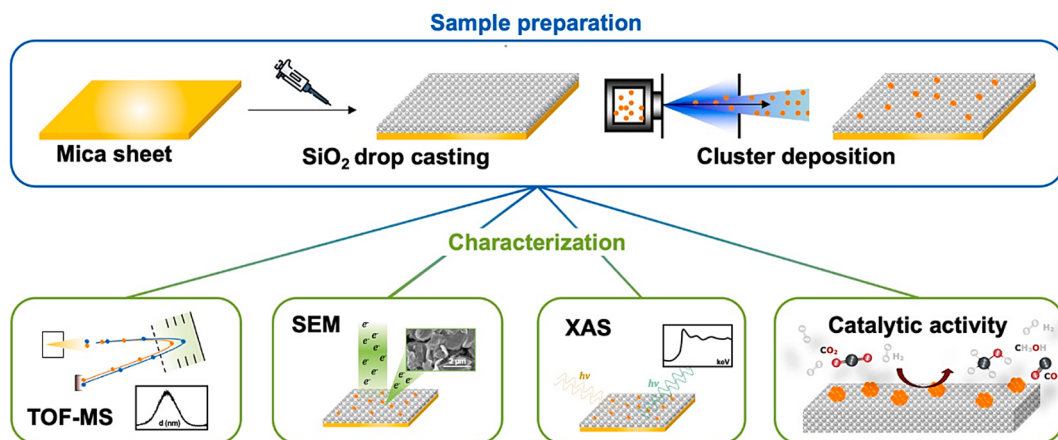


Fig. 2. Schematic representation of the catalyst sample preparation and characterization.

laser (Spectra Physics, INDI, 532 nm, 10 Hz), which generates vapors corresponding to the composition of the target. Simultaneously, a 5% O<sub>2</sub>/He gas is injected into the source with a backing pressure of 8 bar, which causes cooling of the vapor, resulting in condensation and the formation of clusters within the confined volume (around 1 mL) of the aggregation channel of the source. The cluster-gas mixture exits the confined space of the source through a 1 mm opening nozzle, inducing a supersonic expansion generating a beam consisting of oxidized bimetallic Pd<sub>0.25</sub>Zn<sub>0.75</sub>O<sub>x</sub> nanoclusters. The nanoclusters in the beam are characterized by *in situ* Time-of-Flight Mass Spectrometry (TOF-MS) and their mass distribution is converted into a particle diameter distribution assuming a spherical shape and a weighted average density using the following equation:

$$d = 2 \cdot \sqrt[3]{\frac{3m}{4\pi\rho}} \quad (i)$$

Where  $d$ ,  $m$ , and  $\rho$  are, respectively, the diameter, the mass (determined from TOF-MS), and the density (set equal to the weighted average density of Pd and Zn) of the nanoclusters.

The mass flux of the cluster beam in ng/min/cm<sup>2</sup> was determined using a Quartz Crystal Microbalance (QCM). The flux of the cluster beam was maximized while a narrow nanocluster size distribution was achieved by adjusting laser power, condensation gas pressure, and source temperature. After this optimization, the SiO<sub>2</sub>-coated mica substrates were placed in front of the beam for the nanocluster deposition. Using the measured mass flux,  $\Phi_{ma}$ , the nanocluster loading (ng/cm<sup>2</sup>) is defined by the deposition time,  $t$ . The accuracy of the determined mass loading was found to be  $\pm 5\%$  by comparing it with the results obtained by Inductively Coupled Plasma (ICP) mass spectrometry (see supplementary information, Table S1). The loading in terms of an equivalent height expressed in atomic monolayers,  $h_{ML}$ , was calculated using the following formula:

$$h_{ML}[ML] = \frac{\Phi_{ma}[\text{ng min}^{-1}\text{cm}^{-2}]t[\text{min}]}{258[\text{ng ML}^{-1}\text{cm}^{-2}]} \quad (ii)$$

Where the 258 ng ML<sup>-1</sup> cm<sup>-2</sup> conversion factor is based on the average bulk density and average atom size of Pd and Zn. Each SiO<sub>2</sub>-coated mica sheet was decorated with three 2 cm<sup>2</sup> circular depositions (total area 3 × 2 cm<sup>2</sup> = 6 cm<sup>2</sup>) of Pd<sub>0.25</sub>Zn<sub>0.75</sub>O<sub>x</sub> nanoclusters. The samples were prepared with different loadings: 1)  $m = 2.07 \mu\text{g}/\text{cm}^2 \times 6 \text{ cm}^2 = 12.4 \mu\text{g}$  (or  $h_{ML} = 8.8 \text{ ML}$ ) and 2)  $m = 1.1 \mu\text{g}/\text{cm}^2 \times 6 \text{ cm}^2 = 6.6 \mu\text{g}$  (or  $h_{ML} = 4.7 \text{ ML}$ ). One 2 cm<sup>2</sup> circular deposition was also carried out on carbon paper, an electrically conducting substrate, to facilitate composition analysis using Energy Dispersive X-Ray Spectroscopy (EDX/EDS).

#### 2.4. Deposited catalyst characterization

The surface of the SiO<sub>2</sub>-coated mica sheet modified with Pd<sub>0.25</sub>Zn<sub>0.75</sub>O<sub>x</sub> nanoclusters was characterized using Scanning Electron Microscopy (SEM) with a Thermo Scientific Helios 5 Hydra UX PFIB microscope. The SEM was operated at an acceleration voltage of 5 kV and a current of 0.20 nA. The secondary electrons were collected using a Through-the-Lens Detector (TLD) in immersion mode, and the images were captured with a pixel size of 0.35 nm. Under optimal focus conditions, the probe size is estimated to be approximately 1 nm. EDX/EDS measurements were conducted with a Quanta FEG 250 Analytical ESEM mounting an X-Max50 detector. The acceleration voltage was set to 30 kV, the spot size to 5.5 nm, and the working distance to 10 mm.

The deposited nanoclusters were further analyzed using X-ray absorption spectroscopy (XAS). XAS data were collected at the SAMBA beamline of the French national synchrotron facility SOLEIL in Paris-Saclay, France. The facility is equipped with a Si (220) monochromator cooled with liquid nitrogen. The spectra were recorded at the Pd K-edge (24,357.6 eV) in grazing incidence mode (incidence angle around 1°) using fluorescence detection. A Canberra 35-element detector was used, and the incoming beam was measured with a nitrogen-filled ion chamber. Samples were measured under ambient conditions up to a wavenumber of 11 Å<sup>-1</sup>. The typical acquisition time was six minutes per spectrum in continuous scanning mode. At least six spectra were averaged for each sample using the Athena software to improve data quality. Data reduction of the experimental x-ray absorption spectra was performed with the program EXBROOK and the EXAFS refinements with the EXCURVE package [43].

#### 2.5. Activity testing

The SiO<sub>2</sub>-coated mica sheets decorated with nanoclusters were removed from the cluster deposition apparatus and loaded into the microreactor. These samples were then heated up to the required temperature with a ramp rate of 4 °C/min in a 3H<sub>2</sub>:1CO<sub>2</sub> feed gas at a pressure of 40 bar. Feed gas flow rates were varied from 0.5 to 4 sccm (0.04 to 0.32 sccm/μg<sub>cat</sub>) for flow-rate effect experiments at 200 °C, 220 °C, and 240 °C. To study the pressure effect, the pressure was varied from 5 bar to 40 bar at 240 °C with a 0.5 sccm feed gas flow rate. All the reported data were collected 40–48 h after the start of the reaction to minimize the influence of catalyst deactivation and restructuring on kinetic data. The product lines from the reactor to the GC were heated to avoid the condensation of liquid products. In the GC the products were separated using a PlotQ capillary column and quantified with a Thermal Conductivity Detector (TCD) and a Flame Ionization Detector (FID). The FID is equipped with a methanizer and was operated with air and H<sub>2</sub>, flowing at rates of 350 mL/min and 50 mL/min, respectively.

### 3. Simulation model

Reaction engineering and fluid dynamics simulations, performed with the COMSOL Multiphysics package [44], were used to validate the design and performance of the microreactor. The following governing equations were solved:

#### 3.1. Conservation of mass

$$\frac{dC_j}{dt} = V_r R_j + A_r R_{ads,j} \quad (\text{iii})$$

$$A_r = a_s V_r \quad (\text{iv})$$

Where  $V_r$  is the volume of the reactor ( $\text{m}^3$ ),  $C_j$  is the concentration of species  $j$  in the reactor ( $\text{mol m}^{-3}$ ), and  $R_j$  is the rate of production (or consumption) of species  $j$  per unit volume due to chemical reaction occurring in the bulk ( $\text{mol m}^{-3} \text{s}^{-1}$ ).  $R_j$  is set to zero as the reaction proceeds only on the catalytic surfaces.  $R_{ads,j}$  represents the rate of surface reaction of species  $j$  per unit surface area ( $\text{mol m}^{-2} \text{s}^{-1}$ ).  $A_r$  is the area of catalytic surfaces ( $\text{m}^2$ ) where adsorption/desorption can occur and  $a_s$  is the ratio of  $A_r$  to  $V_r$ .

**Fluid flow:** The fluid flow in the microreactor channel is modelled by solving the continuity equation and the steady state Navier-Stokes equation for incompressible fluids in the ‘Laminar Flow’ interface. The governing equations are as follows:

$$\rho \nabla \cdot \mathbf{u} = 0 \quad (\text{v})$$

$$\rho(\mathbf{u} \cdot \nabla) \mathbf{u} = -\nabla p + \mu \nabla^2 \mathbf{u} + \mathbf{F} \quad (\text{vi})$$

where  $\rho$  is the fluid density ( $\text{kg/m}^3$ ),  $\mathbf{u}$  is the velocity field ( $\text{m/s}$ ),  $p$  is the pressure ( $\text{Pa}$ ),  $\mu$  is the dynamic viscosity ( $\text{Pa}\cdot\text{s}$ ), and  $\mathbf{F}$  represents the external forces per unit volume (e.g., gravity).

The flow in the reactor is controlled by defining the flow rate at the inlet boundary condition, while the pressure is defined at the outlet boundary condition. The flow velocity is zero ( $\mathbf{u} = 0$ ) at the reactor walls. The density and viscosity of air, along with their temperature dependence, are assumed to adequately represent the properties of the reaction gas mixture. The gas mixture is assumed to behave as an ideal gas, and the pressure drop is considered negligible due to the short reactor length and low flow rates.

**Mass transport:** The mass transport is described through the diffusion-convection equation in ‘Transport of Diluted Species’ interface:

$$\frac{\partial C_j}{\partial t} + \nabla \cdot (\mathbf{u} C_j) = \nabla \cdot (D_j \nabla C_j) + R_j \quad (\text{vii})$$

Since the reaction takes place on the catalytic surface, the boundary fluxes for the area covered with the catalyst are given by:

$$-\mathbf{n} \cdot (D_j \nabla C_j) = R_{ads,j} \quad (\text{viii})$$

where  $\mathbf{n}$  is the normal vector to the surface with the catalyst, and  $D_j$  is the diffusion coefficient of species  $j$  ( $\text{m}^2/\text{s}$ ), which was calculated based on the kinetic gas theory using the following expression:

$$D_{AB} = 2.6628 \cdot 10^{-22} \cdot \sqrt{\frac{(T^3(M_A + M_B)/(2 \cdot 10^3 M_A M_B))}{p \sigma_A \sigma_B}} \cdot \Omega_D^{-1} \quad (\text{ix})$$

Here,  $D_{AB}$  ( $\text{m}^2/\text{s}$ ) is the binary diffusion coefficient,  $M$  ( $\text{kg/mol}$ ) is the molecular weight,  $T$  ( $\text{K}$ ) represents the absolute temperature,  $p$  ( $\text{Pa}$ ) the pressure,  $\sigma$  ( $\text{m}$ ) is the characteristic length of the Lennard-Jones/Stockmayer potential,  $\Omega_D$  is the collision integral [45]. Inlet conditions are defined by the inlet concentrations, and at the outlet, the mass transport is dominated by convection, with the diffusive flux set to zero.

Similarly, a no flux condition is applied to all boundaries where the velocity is zero, except at the catalytic surfaces.

#### 3.2. Geometry and mesh

As detailed in Section 2.1 and illustrated in Fig. 3a, the placement of the planar catalyst sample in the microreactor creates a rectangular microchannel measuring  $48 \times 18 \times 0.07 \text{ mm}^3$  (green), with catalyst-deposited surfaces at the bottom of the channel (highlighted by orange dashed circles in Fig. 3b). The inlets and outlets are indicated by white-filled and dark-filled small circles in Fig. 3b at both ends of the channel. A 3D model of the microreactor was developed and discretized using a physics-controlled generation of a free triangular mesh, resulting in a denser mesh on the catalytic surfaces to accurately account for the non-zero boundary flux. Initially, simulations were conducted at a single temperature for the highest and lowest flow rates using a coarser mesh. The mesh density was then systematically adjusted until the results became independent of further increases in mesh density. Finally, all simulations were performed using a ‘fine’ mesh comprising 2,561,479 domain elements, 716,140 boundary elements, and 5,910 edge elements. An enlarged view ( $15\times$ ) of a corner of the discretized domain, shown in Fig. 3c, demonstrates the mesh generation used for the simulations.

#### 3.3. Simulation Strategy

To simulate the reaction occurring on catalytic surfaces, a surface species,  $\text{AS}_{(ads)}$ , representing the catalyst deposited on the catalytic surface, was introduced as both a reactant and product. The concentration of  $\text{AS}_{(ads)}$  was set constant during the simulations. The reaction was simulated using a space-independent model, and the resulting chemical data were then exported to a space-dependent model of the microreactor (the domain shown in Fig. 3). In the space-dependent model, the transport of diluted species and laminar flow were set up to describe the mass and momentum transport within the reacting system. The model was first solved for fluid flow, followed by the calculation of the mass transport using the fluid field to represent convection of the gases.

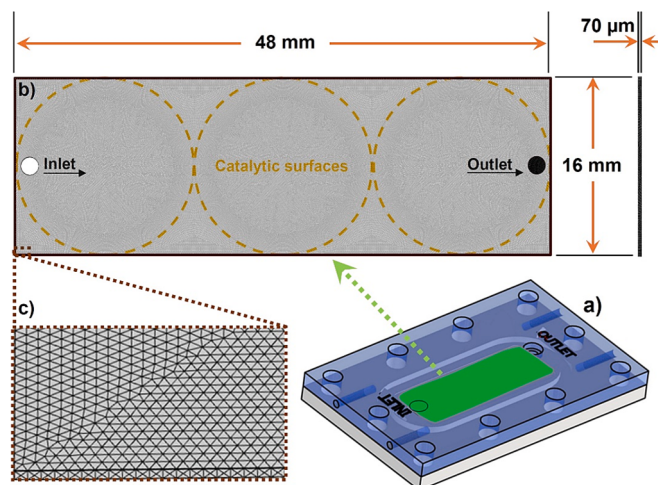
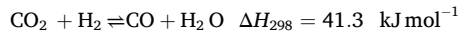


**Fig. 3.** (a) 3D representation of the microreactor, with the green part representing the microchannel; (b) 2D diagrams of the microchannel domain built for the simulations. Large, dashed circles indicate catalytic surfaces, while the small white-filled and dark-filled circles represent the inlet and outlet, respectively; (c) Enlarged view ( $15\times$ ) of a section of the free triangular mesh of the domain. (For interpretation of the references to colour in this figure legend, the reader is referred to the web version of this article.)

## 4. Results and discussions

### 4.1. Kinetic model

As most of the reacted  $\text{CO}_2$  was found to be converted to CO, *vide infra*, competing reactions are ignored in the kinetic model, and we evaluate the reactor performance using the RWGS reaction only:



Without a good understanding of the active sites and the RWGS reaction mechanism over the prepared catalysts, it is difficult to apply the traditional Langmuir–Hinshelwood model [46]. However, a power-law rate expression with an Arrhenius equation is sufficient in predicting the operating conditions and evaluating the reactor design.

For very low conversions, the backward reaction can be neglected, and the RWGS reaction rate can be expressed in terms of the CO formation rate:

$$R_{\text{CO}} = k(C_{\text{CO}_2})^\alpha(C_{\text{H}_2})^\beta \quad (\text{x})$$

Where:

- $R_{\text{CO}}$  is the rate of CO formation ( $\text{mol m}^{-3} \text{s}^{-1}$ )
- $C_{\text{CO}_2}$  and  $C_{\text{H}_2}$  are the concentrations of carbon dioxide and hydrogen ( $\text{mol m}^{-3}$ )
- $\alpha$  and  $\beta$  are the partial orders of reaction with respect to  $\text{CO}_2$  and  $\text{H}_2$ , respectively.

- $k$  is the rate constant ( $[\text{mol m}^{-3}]^{1-\alpha-\beta} \text{ s}^{-1}$ ) and is given by the Arrhenius equation:

$$k = Ae^{\frac{-E_a}{RT}} \quad (\text{xi})$$

- $A$  is the pre-exponential or frequency factor and has the same units as  $k$
- $E_a$  is the activation energy ( $\text{J mol}^{-1}$ )
- $R$  is the gas constant (approximately  $8.314 \text{ J mol}^{-1}\text{K}^{-1}$ )
- $T$  is the absolute temperature (K)

For  $\text{H}_2$ -rich feed gas compositions, it was shown that the partial reaction order with respect to hydrogen,  $\beta$ , reaches zero [47,48]. Therefore,  $\beta = 0$  was used in our analysis and the final equation becomes:

$$R_{\text{CO}} = Ae^{\frac{-E_a}{RT}}(C_{\text{CO}_2})^\alpha \quad (\text{xii})$$

The expression was fitted to the experimental data to find the kinetic parameters of the rate law.

### 4.2. Catalyst characterization

A precise control of the size, composition, and loading of the catalyst was crucial for evaluating the performance of the microreactor. The size distribution of the nanoclusters in the gas phase characterized by TOF-MS shows an average cluster diameter of  $2.5 \pm 0.8 \text{ nm}$  (Fig. 4b). After

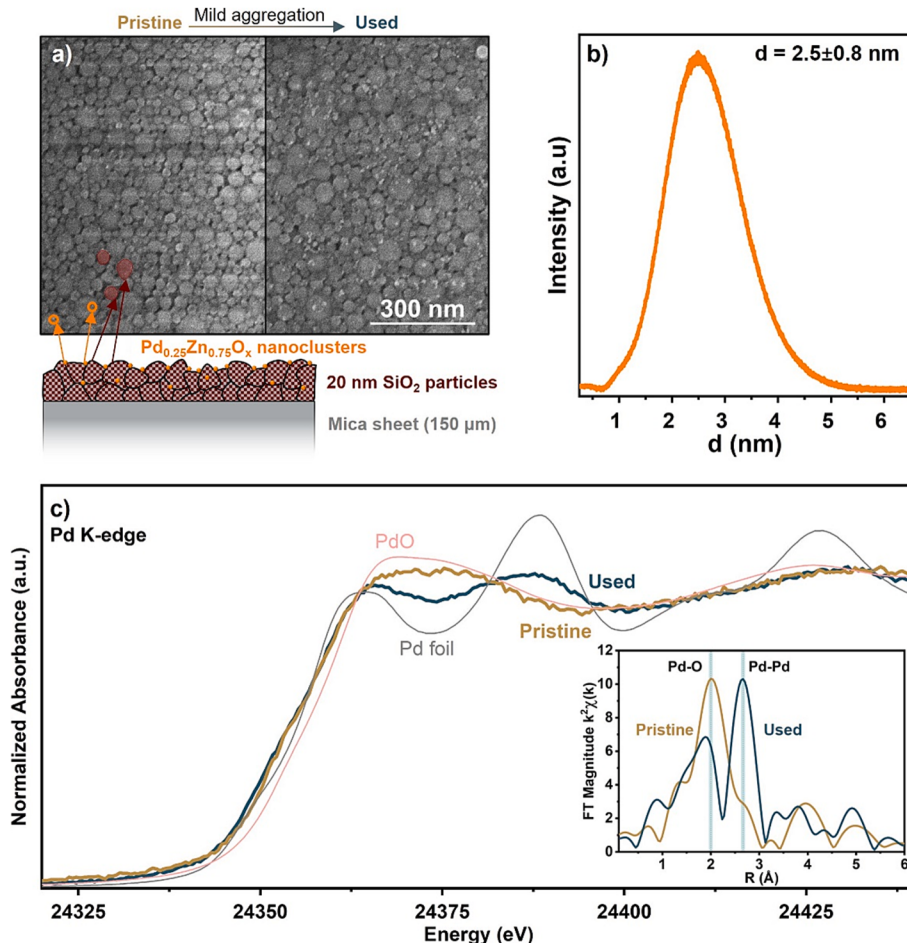


**Fig. 4.** (a) SEM images of the pristine (left) and used (right) samples; (b) TOF-MS nanocluster diameter distribution before deposition, yielding an average diameter of 2.5 nm; (c) Pd K-edge XANES and Fourier transform of  $k^2$ -weighted EXAFS spectra (inset) for the pristine and used samples. PdO and Pd foil references are shown for comparison. The schematic at the bottom of (a) illustrates the cross-section of the samples.

deposition, the Pd:Zn molar ratio was determined to be 25:75 through Energy-Dispersive X-Ray (EDX) Spectroscopy (see [supplementary information](#), [Figure S4](#)).

An SiO<sub>2</sub>-coated mica sheet decorated with 8.8 ML of Pd<sub>0.25</sub>Zn<sub>0.75</sub>O<sub>x</sub> was examined using scanning electron microscopy (SEM) both before and after the reaction. [Fig. 4a](#) depicts a nanostructured planar substrate, with only a few nanoclusters visible on the evenly distributed SiO<sub>2</sub> nanoparticles. This may result from the oxidic nature of the pristine clusters (see below) that may cause them not to appear as bright as their metallic counterparts and/or from the electrical insulating properties of the substrate, which limits the image resolution due to charging effects. At the same time, in case the original 2.5 nm clusters would have aggregated on the surface, this should have led to larger particles visible in SEM images. The fact that no aggregates could be identified in the SEM image suggests that clusters have been successfully stabilized in the pristine sample and highlights the role of SiO<sub>2</sub> in the system.

On the contrary, SEM images of the used samples show some cluster aggregates on the SiO<sub>2</sub> support, suggesting that a fraction of the clusters aggregated during the reaction, while the majority is still below the detection limit of the SEM [49]. The role of SiO<sub>2</sub> in stabilizing the clusters under reaction conditions was further investigated by comparison with a reference sample without SiO<sub>2</sub>. An SEM image of this sample, consisting of 1.2 µg/cm<sup>2</sup> (5 ML) of Pd<sub>0.25</sub>Zn<sub>0.75</sub>O<sub>x</sub> nanoclusters directly deposited on a mica sheet and exposed to reaction conditions, demonstrated significant aggregation (see [supplementary information](#), [Figure S5](#)). Atomically flat mica provides minimal surface roughness and the effective surface area available to support the nanoclusters is essentially the same as the geometric area. This results in clusters being deposited close to each other even at such low loadings. This proximity, combined with their mobility on the surface, increases the likelihood of nanocluster aggregation [50,51]. By increasing the surface roughness, SiO<sub>2</sub> coating does not only limit the mobility of the nanoclusters by creating physical barriers to the movement but also increases the effective surface area reducing the chance of clusters coming into close contact and significantly minimizing their aggregation.

XANES spectra of pristine and used Pd<sub>0.25</sub>Zn<sub>0.75</sub>O<sub>x</sub>, measured at the Pd K-edge ([Fig. 4c](#)), confirm the presence of clusters on the SiO<sub>2</sub>-coated mica sheets and show two distinct profiles that resemble the PdO reference for a pristine sample and the Pd foil for the used one. The damped oscillations in the used sample compared to the Pd foil confirm the nanoscopic character of the catalyst. Phase-corrected Fourier Transforms of Pd K-edge k<sup>2</sup>-weighted EXAFS ([Fig. 4c](#) insert) of pristine and used Pd<sub>0.25</sub>Zn<sub>0.75</sub>O<sub>x</sub> nanoclusters feature distinct profiles in line with the XANES analysis. The pristine Pd<sub>0.25</sub>Zn<sub>0.75</sub>O<sub>x</sub> spectrum has a peak at 2 Å corresponding to a Pd-O contribution, while the peak at 2.7 Å corresponds to a Pd-Pd and/or a Pd-Zn distance. The EXAFS analysis (see [supplementary information](#), [Figure S2](#) and [Table S4](#)) shows that the first peak of the pristine Pd<sub>0.25</sub>Zn<sub>0.75</sub>O<sub>x</sub> corresponds to 3.4 oxygen atoms at 2.01 Å, indicating that it consists of 85 % of PdO while the remaining part, likely Pd<sup>0</sup>, could not be detected in the fit. After the reaction, the Pd-O contribution is reduced to 0.8 at 1.99 Å corresponding to only 20 % of PdO, while the main FT peak could be fitted with a combination of 7.6 Pd at 2.69 Å and 1.8 Zn at 2.62 Å suggesting the formation of a random Pd-rich PdZn alloy containing ca. 20 % of Zn. The remaining Zn fraction is expected to be ZnO. As the samples were stored in the ambient after the reaction, the oxide fraction in the used samples may originate from post-reaction transformation.

These characterizations of the deposited nanoclusters show that they remain in the nanometer size range with limited aggregation, highlighting the role of the SiO<sub>2</sub> coating on the mica sheet in minimizing the mobility of the clusters. This is further evidenced by the stable activity of the prepared catalysts, as discussed in the following sections. At the same time, the structural and chemical changes occurring in the system – namely, the shift from a mostly fully oxidized form in the pristine sample to a PdZn alloy in the used sample – highlight a restructuring occurring under the reaction conditions.

#### 4.3. Catalytic activity

[Fig. 5a](#) presents the product concentrations at the microreactor exit, measured with the online GC, during an experiment conducted using 8.8 ML of Pd<sub>0.25</sub>Zn<sub>0.75</sub>O<sub>x</sub> at 40 bar and 220 °C. Experimental data for the other test conditions are provided in the [supplementary information](#) ([Figure S1](#)).

The results indicate a stable activity under all reaction conditions, demonstrating that the aforementioned mild aggregation of the nanoclusters does not affect the catalyst performance. It also provides evidence that ligand-free nanoclusters prepared in ultra-high vacuum can indeed be mechanically immobilized (e.g., on the rough SiO<sub>2</sub> coating) to enable prolonged catalyst operation.

A summary of the reaction rate and selectivity for each test condition is provided in the [supplementary information](#) ([Table S2](#)). The reaction rate for CO production ranges from 16.7 mmol g<sub>cat</sub><sup>-1</sup> hr<sup>-1</sup> at 200 °C and 0.5 sccm (or 0.04 sccm/µg<sub>cat</sub>) to 223 mmol g<sub>cat</sub><sup>-1</sup> hr<sup>-1</sup> at 240 °C and 4 sccm (or 0.32 sccm/µg<sub>cat</sub>), with a CO selectivity maintained above 97 % for all the test conditions. These results indicate that the prepared catalyst is highly active and selective towards the CO<sub>2</sub> hydrogenation reaction to produce CO with only trace amounts of MeOH and CH<sub>4</sub>. The high activity, selectivity, and stability make the selected catalyst an ideal choice for conducting control experiments and evaluating the microreactor's performance.

The kinetic parameters of equation (xii) were determined by fitting it to the experimental data. The Arrhenius plots at different specific flow rates ([Fig. 5b](#)) yield an apparent activation energy of  $E_a = 105 \text{ kJ mol}^{-1}$ . This result is consistent with previously reported values of 100 kJ mol<sup>-1</sup> and 120 kJ mol<sup>-1</sup> for the RWGS reaction over CuO/ZnO/Al<sub>2</sub>O<sub>3</sub> [47] and Pd/TiO<sub>2</sub> [52] catalysts, respectively. The reaction order with respect to CO<sub>2</sub> is 0.82, as determined by fitting the pressure dependence (5–40 bar) of the reaction rate at a fixed temperature of 240 °C ([Fig. 5c](#)). [Table 1](#) provides a summary of the obtained kinetic parameters. These parameters were used in COMSOL to simulate and visualize the design and performance of the microreactor.

#### 4.4. Effect of reaction temperature and specific flow rate

The experimental data elucidating the effect of temperature and specific flow rate on the reaction, together with the simulation results, are presented in [Fig. 6a](#) and [6b](#). The data were measured by varying the feed gas flow rate from 0.5 to 4 sccm (0.04 to 0.32 sccm/µg<sub>cat</sub>) at 40 bar and constant reaction temperatures of 200 °C, 220 °C, and 240 °C. The experimentally measured CO concentrations closely match those predicted by the simulations across different temperatures and flow rates. This agreement is illustrated in the parity plot shown in [Fig. 6c](#), which demonstrates a good linear relationship with an R<sup>2</sup> value of 0.995. This indicates that the model proposed in [section 4.1](#) describes the kinetics with high accuracy across the employed range of test conditions.

The results show an exponential increase in CO concentration with rising temperature ([Fig. 6a](#)) for all flow rates. This behaviour is further confirmed by the consistent values of apparent activation energies of 105 – 106 kJ/mol obtained from the Arrhenius plots ([Fig. 5b](#) and [Table S3](#)). These findings suggest that the used planar substrate and microreactor geometry effectively facilitate the reaction without significant heat and mass transfer limitations across a wide range of testing conditions.

[Fig. 6b](#) illustrates the CO concentration at the reactor exit as a function of the specific flow rate at different temperatures. At all temperatures, the increase in the flow rate leads to an exponential decrease in the product concentration. This can be explained by the shorter contact time between reactants (CO<sub>2</sub> and H<sub>2</sub> molecules) and the catalytic surface resulting in lower conversion rates and, consequently, lower CO concentrations at the microreactor exit.

A slight increase in the reaction rate with the rising feed gas flow rate is observed ([Fig. 6d](#)) at all temperatures. Several factors could contribute

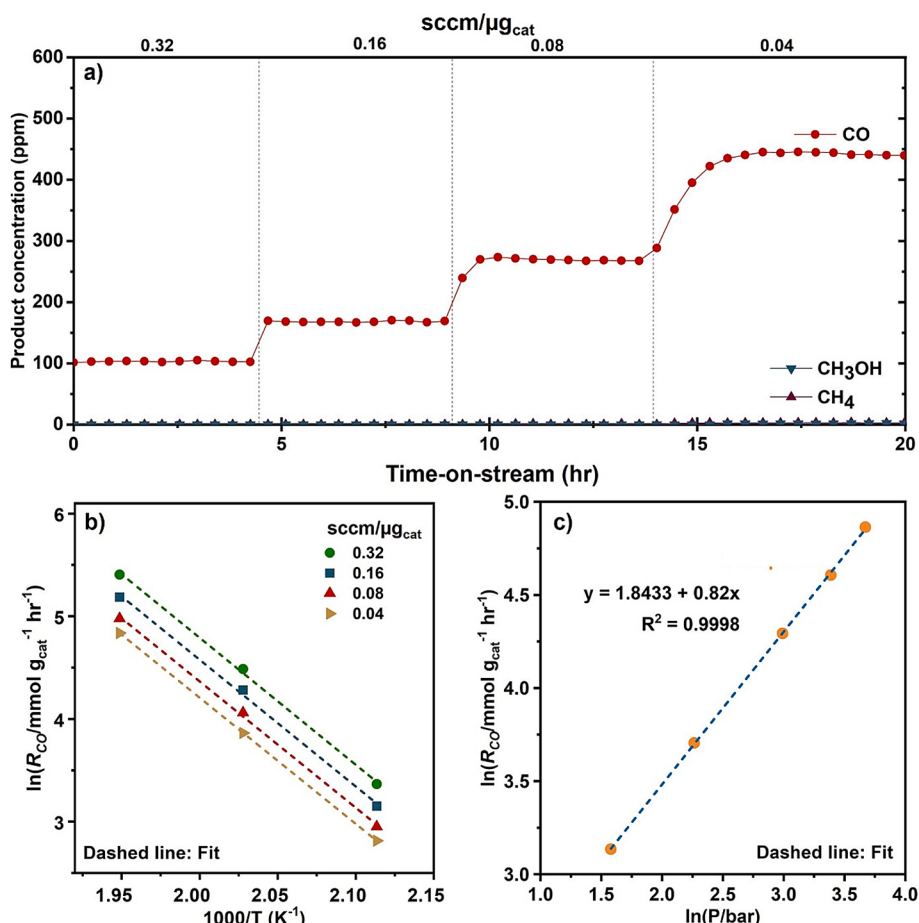


**Fig. 5.** (a) Product concentrations measured at 40 bar, 220 °C and various specific flow rates of the 3H<sub>2</sub>:1CO<sub>2</sub> feed gas, using a 2.1 μg/cm<sup>2</sup> loading of Pd<sub>0.25</sub>Zn<sub>0.75</sub>O<sub>x</sub> catalyst; (b) Arrhenius plots for CO formation at different specific flow rates, illustrating the consistent temperature dependence of the reaction rate and allowing determination of the activation energy; (c) Reaction order with respect to CO<sub>2</sub> determined using data collected at 240 °C and for pressures varying between 5 and 40 bar.

**Table 1**  
Kinetic parameters for reverse water–gas shift reaction over Pd<sub>0.25</sub>Zn<sub>0.75</sub>O<sub>x</sub>.

Model	k	A ([mol m <sup>-3</sup> ] <sup>0.18</sup> s <sup>-1</sup> )	E <sub>a</sub> (kJ/mol)	Reaction order α
Power-Law	$A \cdot \exp(-E_a/RT)$	605 ± 5	105.4 ± 0.2	0.82 ± 0.01

to this behavior, including product inhibition, changes in mass transport limitations, and a non-linear decrease in residence time distribution.

The product inhibition has been reported for several catalysts [53–56] and it could lead to a change in the reaction rates with varying flow rates. At lower flow rates, a higher concentration of both water and CO can accumulate in the vicinity of the nanoclusters. Additional adsorption sites provided by SiO<sub>2</sub> coating of mica sheet may further enhance this effect. The buildup can promote the backward reaction, reducing the net rates of CO formation at lower flow rates. As the flow rate increases, enhanced sweep and turbulence can remove adsorbed water more effectively, thus reducing product inhibition. At the same time, this effect is dependent on both temperature and product concentration.

In the current study, increasing the flow rate eightfold, from 0.04 to 0.32 sccm/μg<sub>cat</sub>, resulted in reaction rate increases by factors of 1.74, 1.86, and 1.77 at 200 °C, 220 °C, and 240 °C, respectively. This indicates that the extent of the increase of the reaction rate as a function of flow rate is essentially independent of the temperature and the product

concentrations. Therefore, the influence of product inhibition on the reaction rate is excluded.

Similar reasoning can be applied to demonstrate the absence of mass transport limitations. A detailed analysis presented in Section 4.5 will prove that the reaction does not occur in the mass transport-limited regime. Therefore, the increase in the reaction rate at higher flow rates can be attributed to non-linear changes in the residence time distribution. In an ideal plug flow reactor, all the fluid molecules spend equal time inside the reactor and increasing the flow rate linearly decreases the residence time of the reactants. In the current scenario, internal mixing and recirculation are expected due to higher gas velocities near the inlet and outlet. This would cause a non-linear change in residence time with increasing flow rate. These effects would also be independent of the changes in temperature and are in line with our observations of the consistent reaction rate change across all temperatures.

#### 4.5. Mass transport study

As gas passes through the microreactor channel, which has a height of 70 μm, it establishes a parabolic velocity profile due to the no-slip condition at the walls. This results in a maximum velocity at the center of the channel, which decreases to zero at the reactor walls, including the catalytic surfaces (Fig. 7a). Consequently, the reactants must diffuse from the bulk flow to the surface of the catalyst through a stagnant fluid layer. Similarly, products formed on the catalytic surface will diffuse back through this stagnant layer to enter the bulk flow and exit the

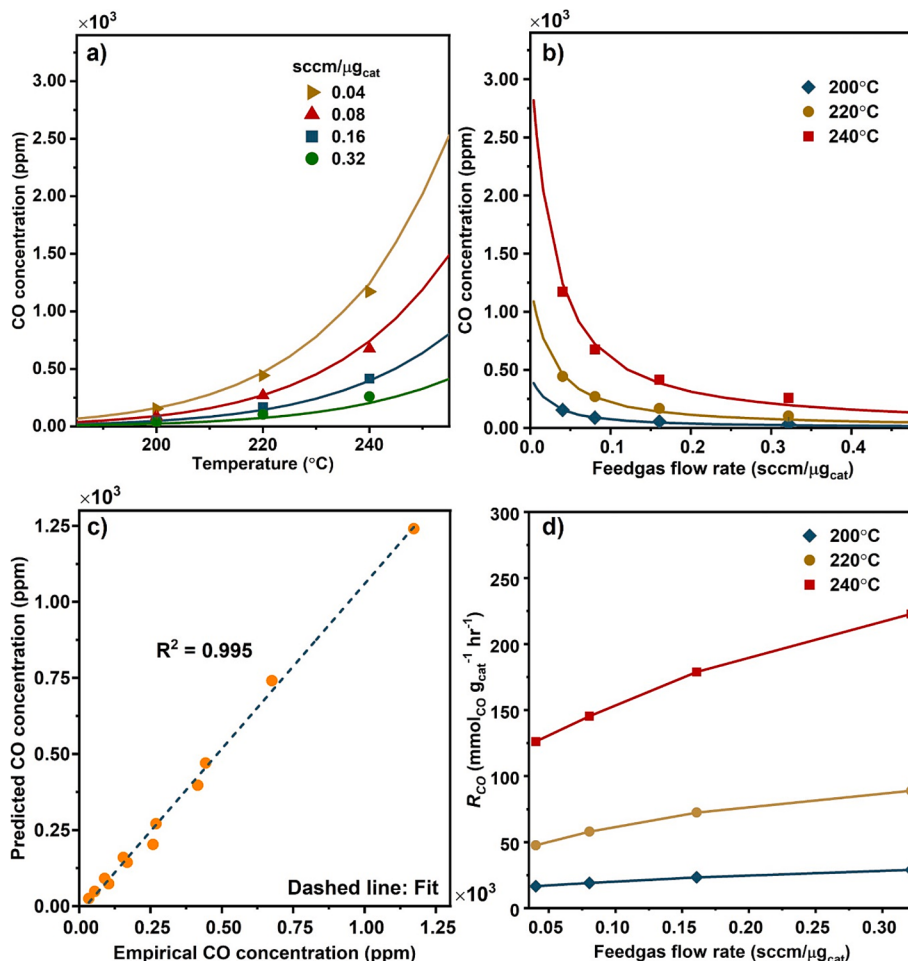


**Fig. 6.** Predicted (lines) and experimental (symbols) CO concentrations measured at the microreactor exit during reactions conducted at 40 bar plotted as a function of (a) temperature and (b) specific flow rate; (c) Parity plot comparing all experimental and predicted CO concentrations; (d) Dependence of the experimental CO formation rate on specific flow rates at different temperatures.

microreactor. This diffusion process is crucial for determining whether the reaction is kinetically controlled or limited by mass transport.

For a reaction to be governed by kinetic control, the diffusion rate through the stagnant layer should be higher than the catalytic reaction rate. If this condition is not met, a reactant deficiency at the catalyst surface occurs, shifting control over the reaction rate to diffusion processes. Such a scenario hinders the investigation of true kinetics, as its details would be masked by diffusion limitations.

The experimental data from this study indicate a maximum reaction rate of  $1.61 \times 10^{13}$  molecules cm<sup>-2</sup> s<sup>-1</sup> at 240 °C, 40 bar, and 0.5 sccm. The diffusion rate of water, the slowest diffusing product, is 8 orders of magnitude higher than the observed reaction rate, assuming a concentration gradient of just 10 ppm across the stagnant layer of 35 μm thickness and  $10^{-5}$  m<sup>2</sup>/s diffusion coefficient of water at those conditions [57]. This substantial difference indicates that diffusion should be significantly faster than the reaction rate.

To get further insight into the mass transport, characteristic time scales and dimensionless numbers are defined and provided in Table 2.

The Peclet number ( $Pe$ ) and Damköhler number II ( $Da_{II}$ ), calculated for the reaction conditions in the microreactor channel, provide further evidence of an absence of transport limitations. Previous microfluidics studies have established that species concentrations remain uniform across the channel height when  $Pe$  and  $Da_{II}$  are less than unity [58]. The calculated values for these parameters (Table 2) indicate that diffusion is sufficiently rapid to ensure uniform species distribution and that reaction kinetics predominate over diffusion limitations.

To experimentally verify the absence of diffusion limitations across the stagnant layer over the catalyst surface, the reaction rates for two different catalyst loadings were compared under the experimental conditions that are most susceptible to mass transfer limitations (240 °C, 40 bar, 0.5 sccm). The observed reaction rate for 4.7 ML and 8.8 ML catalyst loadings were equal to 126 and 130 mmol g<sub>cat</sub><sup>-1</sup> hr<sup>-1</sup>, respectively. The observation of very similar reaction rates for different catalyst loadings further proves the absence of mass transfer limitations. Therefore, we conclude that the reactor geometry is suitable for studying the kinetics of minute amounts of catalysts deposited on planar substrates. Additionally, the consistent activation energy at various flow rates and the stable dependence of reaction rate on pressure (Fig. 5b and 5c) confirm that the reaction kinetics can be extracted in a reliable manner using the microreactor setup.

#### 4.6. Concentration profiles

The concentration profiles of CO at 240 °C and 40 bar are presented in Fig. 7b and 7c for the lowest and highest flow rates (0.04 and 0.32 sccm/μg<sub>cat</sub>, respectively). The simulation provides a detailed insight into the distribution of product along the length and width of the microreactor channel. These profiles reveal that the product concentration continuously increases from the inlet to the outlet of the reactor. Notably, the CO concentration is nearly constant along the width of the channel. These factors collectively indicate a close resemblance to an ideal plug flow reactor [59].

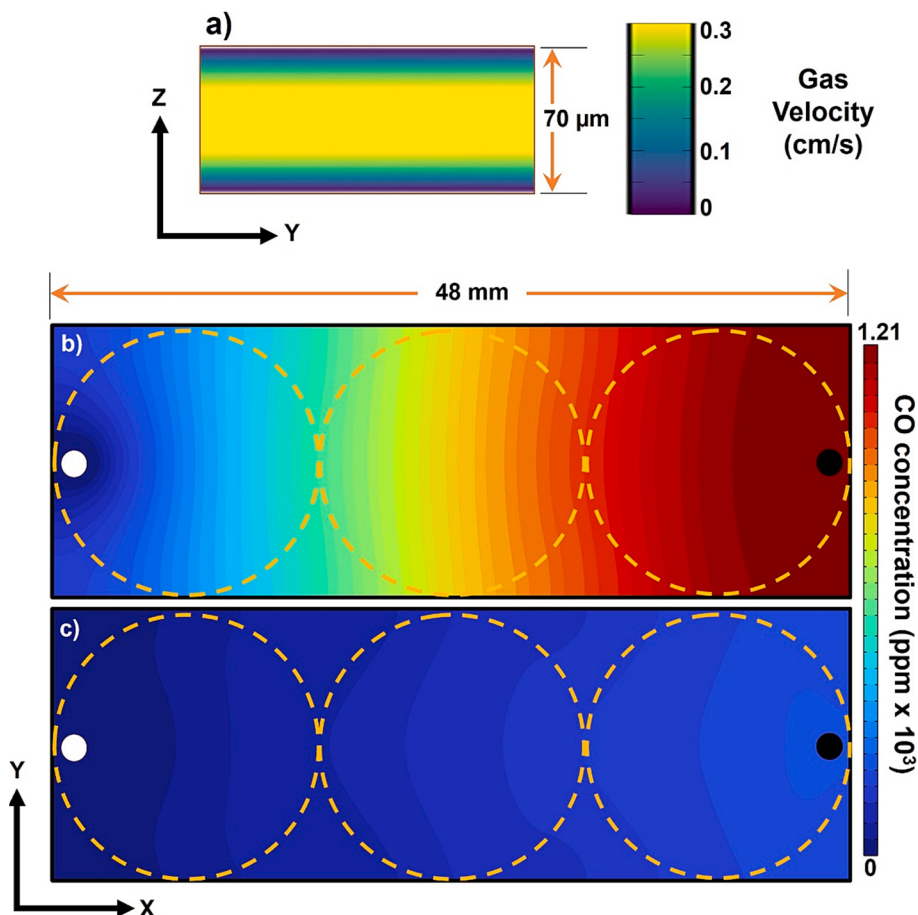


**Fig. 7.** Simulated (a) contour of the velocity magnitude in the microreactor channel, (b) CO concentration profile in the microreactor channel during the RWGS reaction at 40 bar and 240 °C, at 0.04 sccm/μg<sub>cat</sub>, and (c) at 0.32 sccm/μg<sub>cat</sub>. The inlet of the microreactor channel is marked with a white-filled circle, while a dark-filled circle indicates the outlet. The positions of the catalyst surfaces within the microreactor channel are represented by dashed orange circles. (For interpretation of the references to colour in this figure legend, the reader is referred to the web version of this article.)

**Table 2**  
Characteristic time scales and dimensionless numbers for mass transfer study.

Parameter	Symbol	Definition	Value
Gas flow rate at reaction conditions (cm <sup>3</sup> /min)	$v_0$	sccm × T $273.15 \times P$	0.022–0.194
Mean Residence time (s)	$\tau$	$V_{\mu r}/v_0$	15.5–138.5
Max diffusion time (s)	$t_D$	$h_2/D$	$2.4 \times 10^{-4}$
Peclet number	$Pe$	$t_D/\tau$	$1.7-15 \times 10^{-6}$
Damköhler number	$Da$	$\frac{R_{CO} \times V_{\mu r}}{F_{CO_2}}$	$3.7-126 \times 10^{-4}$
Damköhler number II	$Da_{II}$	$\tau/t_D$	$3-42 \times 10^{-9}$

#### 4.7. Microreactor sensitivity

The high sensitivity of the microreactor is achieved through an accurate control of the low flow rates supplied to the 50 μL reactor channel through low dead volume capillaries and a sensitive product quantification down to 1 ppm via a GC. In the current experiments, with a feed gas flow rate of 0.5 sccm, temperature of 240 °C, and pressure of 40 bar, the CO concentration measured at the reactor exit was 1172 ppm and 645 ppm for samples with catalyst loadings of 2.1 μg/cm<sup>2</sup> (8.8 ML) and 1.1 μg/cm<sup>2</sup> (4.7 ML), respectively. This demonstrates a proportional relationship between catalyst loading and product concentration. By systematically decreasing the catalyst loading under the same conditions, CO concentrations of 50 ppm and 5 ppm at the reactor exit should be observed at catalyst loadings of 160 ng/cm<sup>2</sup> (0.7 ML) and 16 ng/cm<sup>2</sup> (0.07 ML), respectively. To confirm the validity of these estimates, a

standard trace gas mixture containing 5 ppm of various products was passed through the reactor capillaries, and the quantification of CO, methanol, and methane was found to be  $6.0 \pm 1.0$  ppm,  $5.3 \pm 0.5$  ppm, and  $6.6 \pm 1.3$  ppm, respectively, with the error indicating the standard deviation for 10 measurements. Based on these results, we can conclude that the microreactor setup can be used in activity tests with catalyst loadings down to a few hundred nanograms with reasonably high accuracy, even if the mass activity is an order of magnitude lower than in the current study.

#### 5. Conclusions

We present a novel microreactor design for high-pressure catalytic investigations of minute quantities of catalysts deposited on planar substrates. Using the reverse water–gas shift (RWGS) reaction over Pd<sub>0.25</sub>Zn<sub>0.75</sub>O<sub>x</sub> nanoclusters as a model system, we explored the performance of this new microreactor at pressures up to 40 bar and temperatures up to 240 °C. The highly pure, ligand-free Pd<sub>0.25</sub>Zn<sub>0.75</sub>O<sub>x</sub> nanoclusters were prepared using the cluster beam deposition technique in ultra-high vacuum and soft-landed on SiO<sub>2</sub>-coated mica sheets. These substrates provided an excellent support, stabilizing the nanoclusters during tests at high temperature and pressure. The prepared catalysts exhibited high activity (up to 220 mmol g<sub>cat</sub><sup>-1</sup> hr<sup>-1</sup>) and selectivity (up to 97 %) towards CO from CO<sub>2</sub> hydrogenation, making them ideal for conducting controlled experiments aimed at evaluating the microreactor performance.

A rigorous evaluation was achieved through kinetic experiments

carried out under varying reaction conditions. The effect of temperature, pressure, feed gas flow rate, and catalyst loading on reaction, along with the analysis of characteristic dimensionless numbers and COMSOL simulations, offered insights into mass transport, concentration profiles, and the sensitivity of the catalytic measurements conducted in the microreactor. The presented results highlight the capabilities of the reactor to investigate the kinetics of minute quantities of catalysts deposited on planar supports. Catalysts can be prepared using various methods, including drop casting, spin coating, dip coating, and electrodeposition. However, the setup is particularly suitable for fundamental studies using well-defined catalysts prepared through physical methods in ultra-high vacuum. This approach could help bridge the surface science and applied catalysis approaches to catalyst development. A promising application is conducting essential investigations with composition-controlled size-selected nanoparticles prepared through gas-phase cluster beam deposition techniques. These nanoparticles could serve as precise model catalysts to develop reliable structure–activity relationships crucial for the rational design of catalysts for strategically important chemical reactions.

#### Author contributions

I.A., E.J., D.G., and P.L. conceived the idea. I.A. designed the microreactor, executed the installation, and performed the experiments. F.R. and K.P. conducted the SEM and EDS characterization. I.A., K.P., F.R., and D.G. performed X-ray Absorption Spectroscopy measurement. I.A. and D.G. analyzed the data. S.K., C.D., and J.K. contributed to the discussions. I.A. performed COMSOL simulations and wrote the manuscript with feedback from all the authors.

#### CRediT authorship contribution statement

**Imran Abbas:** Writing – review & editing, Writing – original draft, Visualization, Methodology, Investigation, Formal analysis, Conceptualization. **Filippo Romeggio:** Writing – review & editing, Visualization, Formal analysis. **Kacper Pilarczyk:** Writing – review & editing, Validation. **Simon Kuhn:** Writing – review & editing, Validation. **Christian Danvad Damsgaard:** Writing – review & editing, Supervision. **Jakob Kibsgaard:** Writing – review & editing. **Peter Lievens:** Writing – review & editing, Resources, Conceptualization. **Didier Grandjean:** Writing – review & editing, Supervision, Funding acquisition, Formal analysis, Conceptualization. **Ewald Janssens:** Writing – review & editing, Validation, Supervision, Resources, Funding acquisition, Conceptualization.

#### Declaration of competing interest

The authors declare that they have no known competing financial interests or personal relationships that could have appeared to influence the work reported in this paper.

#### Acknowledgements

The authors are grateful to Philippe Mispelter (KU Leuven) for his help in fabricating the microreactor, João Coroa and Jinlong Yin (Teer Coatings Ltd, UK) for providing inert coatings and Olga Safonova (Paul Scherrer Institute, Switzerland) and Christophe Copéret (ETH Zürich) for their valuable suggestions during the project.

This work has received funding from the European Union's Horizon 2020 research and innovation program under grant agreement No. 955650 (CATCHY). The authors also thank the French National Synchrotron, Soleil, for providing beamtime (20231905) and the staff of the SAMBA beamline for their assistance. K.P. acknowledges support from the Polish National Agency for Academic Exchange (project BPN/BEK/2021/1/00374) and the Polish Ministry of Science and Higher Education (scholarship 502765). E.J. acknowledges the Research Foundation Flanders (FWO) for a sabbatical bench fee (K800124N).

#### Appendix A. Supplementary data

Supplementary data to this article can be found online at <https://doi.org/10.1016/j.cej.2024.158127>.

#### Data availability

Data will be made available on request.

#### References

- [1] K. Zhang, D. Guo, X. Wang, Y. Qin, L. Hu, Y. Zhang, R. Zou, S. Gao, Sustainable CO<sub>2</sub> management through integrated CO<sub>2</sub> capture and conversion, *J. CO<sub>2</sub> Util.* 72 (2023) 102493, <https://doi.org/10.1016/j.jcou.2023.102493>.
- [2] A. Parekh, G. Chaturvedi, A. Dutta, Sustainability analyses of CO<sub>2</sub> sequestration and CO<sub>2</sub> utilization as competing options for mitigating CO<sub>2</sub> emissions, *Sustain. Energy Technol. Assessments.* 55 (2023) 102942, <https://doi.org/10.1016/j.seta.2022.102942>.
- [3] R.P. Ye, J. Ding, W. Gong, M.D. Argyle, Q. Zhong, Y. Wang, C.K. Russell, Z. Xu, A. G. Russell, Q. Li, M. Fan, Y.G. Yao, CO<sub>2</sub> hydrogenation to high-value products via heterogeneous catalysis, *Nat. Commun.* 10 (2019) 5698, <https://doi.org/10.1038/s41467-019-13638-9>.
- [4] K.B. Tan, K. Xu, D. Cai, J. Huang, G. Zhan, Rational design of bifunctional catalysts with proper integration manners for CO and CO<sub>2</sub> hydrogenation into value-added products: A review, *Chem. Eng. J.* 463 (2023) 142262, <https://doi.org/10.1016/j.cej.2023.142262>.
- [5] L.Q. Qiu, H.R. Li, L.N. He, Incorporating Catalytic Units into Nanomaterials: Rational Design of Multipurpose Catalysts for CO<sub>2</sub> Valorization, *Acc. Chem. Res.* 56 (2023) 2225–2240, <https://doi.org/10.1021/acs.accounts.3c00316>.
- [6] V. Mehrab, E. Huang, R. Shi, N. Rui, R. Rosales, I. Waluyo, A. Hunt, P. Liu, J. A. Rodriguez, Microscopic Investigation of H<sub>2</sub> Reduced CuO<sub>x</sub>/Cu(111) and ZnO/CuO<sub>x</sub>/Cu(111) Inverse Catalysts: STM, AP-XPS, and DFT Studies, *ACS Catal.* 13 (2023) 9857–9870, <https://doi.org/10.1021/acscatal.3c02514>.
- [7] A. Beck, M. Zabilskiy, M.A. Newton, O. Safonova, M.G. Willinger, J.A. van Bokhoven, Following the structure of copper-zinc-alumina across the pressure gap in carbon dioxide hydrogenation, *Nat. Catal.* 4 (2021) 488–497, <https://doi.org/10.1038/s41929-021-00625-x>.
- [8] L. Österlund, Pressure Gaps in Heterogeneous Catalysis, in: *Heterog. Catal.*, John Wiley & Sons, Ltd, 2021: pp. 225–251. 10.1002/9783527813599.ch13.
- [9] S. Chen, F. Xiong, W. Huang, Surface chemistry and catalysis of oxide model catalysts from single crystals to nanocrystals, *Surf. Sci. Rep.* 74 (2019) 100471, <https://doi.org/10.1016/j.surrep.2019.100471>.
- [10] S.W. Lee, M.L. Luna, N. Berdunov, W. Wan, S. Kunze, S. Shaikhutdinov, B. R. Cuena, Unraveling surface structures of gallium promoted transition metal catalysts in CO<sub>2</sub> hydrogenation, *Nat. Commun.* 14 (2023) 4649, <https://doi.org/10.1038/s41467-023-40361-3>.
- [11] A. Urakawa, Mind the gaps in CO<sub>2</sub>-to-methanol, *Nat. Catal.* 4 (2021) 447–448, <https://doi.org/10.1038/s41929-021-00638-6>.
- [12] A. Beck, V. Paunović, J.A. van Bokhoven, Identifying and avoiding dead ends in the characterization of heterogeneous catalysts at the gas–solid interface, *Nat. Catal.* 6 (2023) 873–884, <https://doi.org/10.1038/s41929-023-01027-x>.
- [13] L. Lu, S. Zou, B. Fang, The Critical Impacts of Ligands on Heterogeneous Nanocatalysis: A Review, *ACS Catal.* 11 (2021) 6020–6058, <https://doi.org/10.1021/acscatal.1c00903>.
- [14] A. Beck, M.A. Newton, L.G.A. van de Water, J.A. van Bokhoven, The Enigma of Methanol Synthesis by Cu/ZnO/Al<sub>2</sub>O<sub>3</sub>-Based Catalysts, *Chem. Rev.* 124 (2024) 4543–4678, <https://doi.org/10.1021/acs.chemrev.3c00148>.
- [15] Q. Tang, G. Hu, V. Fung, D.E. Jiang, Insights into Interfaces, Stability, Electronic Properties, and Catalytic Activities of Atomically Precise Metal Nanoclusters from First Principles, *Acc. Chem. Res.* 51 (2018) 2793–2802, <https://doi.org/10.1021/acs.accounts.8b00380>.
- [16] L. Zhang, Y. Ren, W. Liu, A. Wang, T. Zhang, Single-atom catalyst: A rising star for green synthesis of fine chemicals, *Natl. Sci. Rev.* 5 (2018) 653–672, <https://doi.org/10.1093/nsr/nwy077>.
- [17] R.T. Vang, A Surface Science Approach to Catalysis, *Doctoral dissertation, University of Aarhus, Denmark*, 2005.
- [18] Y. Xia, Y. Xiong, B. Lim, S.E. Skrabalak, Shape-controlled synthesis of metal nanocrystals: Simple chemistry meets complex physics? *Angew. Chemie - Int. Ed.* 48 (2009) 60–103, <https://doi.org/10.1002/anie.200802248>.
- [19] R. Meyer, C. Lemire, S.K. Shaikhutdinov, H.J. Freund, Surface chemistry of catalysis by gold, *Gold Bull.* 37 (2004) 72–124, <https://doi.org/10.1007/BF03215519>.
- [20] M.D. Rötzer, M. Krause, T. Hinke, K. Bertrang, F.F. Schweinberger, A.S. Crampton, U. Heiz, Same size, same support, same spectator? Selective acetylene hydrogenation on supported Pd nanoparticles, *Phys. Chem. Chem. Phys.* 26 (2024) 13740–13750, <https://doi.org/10.1039/d4cp00719k>.
- [21] K. Zhang, A. Cao, L.H. Wandall, J. Vernieres, J. Kibsgaard, J.K. Nørskov, I. Chorkendorff, Spin-mediated promotion of Co catalysts for ammonia synthesis, *Science (80-.).* 383 (2024) 1357–1363. 10.1126/science.adn0558.
- [22] Z. Zhang, T. Masubuchi, P. Sautet, S.L. Anderson, A.N. Alexandrova, Hydrogen Evolution on Electrode-Supported Pt<sub>n</sub> Clusters: Ensemble of Hydride States Governs the Size Dependent Reactivity, *Angew. Chemie Int. Ed.* 62 (2023), <https://doi.org/10.1002/anie.202218210> e202218210.

- [23] R. Cai, F. Martelli, J. Vernieres, S. Albonetti, N. Dimitratos, C. Tizaoui, R.E. Palmer, Scale-up of cluster beam deposition to the gram scale with the matrix assembly cluster source for heterogeneous catalysis (catalytic ozonation of nitrophenol in aqueous solution), *ACS Appl. Mater. Interfaces*. 12 (2020) 24877–24882, <https://doi.org/10.1021/acsmami.0c05955>.
- [24] V.C. Chinnabathini, F. Dingenen, R. Borah, I. Abbas, J. van der Tol, Z. Zarkua, F. D'Acipiti, T.H.T. Nguyen, P. Lievens, D. Grandjean, S.W. Verbruggen, E. Janssens, Gas phase deposition of well-defined bimetallic gold-silver clusters for photocatalytic applications, *Nanoscale*. 15 (2023) 6696–6708, <https://doi.org/10.1039/D2NR07287D>.
- [25] T.R. Henriksen, J.L. Olsen, P. Vesborg, I. Chorkendorff, O. Hansen, Highly sensitive silicon microreactor for catalyst testing, *Rev. Sci. Instrum.* 80 (2009) 124101, <https://doi.org/10.1063/1.3270191>.
- [26] R.E. Tankard, F. Romeggio, S.K. Akazawa, A. Krabbe, O.F. Sloth, N.M. Secher, S. Colding-Fagerholt, S. Helyveg, R. Palmer, C.D. Damsgaard, J. Kibsgaard, I. Chorkendorff, Stable mass-selected  $\text{AuTiO}_x$  nanoparticles for CO oxidation, *Phys. Chem. Chem. Phys.* 26 (2024) 9253–9263, <https://doi.org/10.1039/d4cp00211c>.
- [27] F. Romeggio, J.F. Schouenborg, P.C.K. Vesborg, O. Hansen, J. Kibsgaard, I. Chorkendorff, C.D. Damsgaard, Magnetron Sputtering of Pure  $\delta\text{-Ni}_3\text{Ga}_3$  Thin Films for CO<sub>2</sub> Hydrogenation, *ACS Catal.* 14 (2024) 12592–12601, <https://doi.org/10.1021/acscatal.4c03345>.
- [28] C. Liu, B. Yang, E. Tyo, S. Seifert, J. Debartolo, B. Von Issendorff, P. Zapol, S. Vajda, L.A. Curtiss, Carbon Dioxide Conversion to Methanol over Size-Selected Cu<sub>4</sub> Clusters at Low Pressures, *J. Am. Chem. Soc.* 137 (2015) 8676–8679, <https://doi.org/10.1021/jacs.5b03668>.
- [29] S. Lee, B. Lee, S. Seifert, S. Vajda, R.E. Winans, Simultaneous measurement of X-ray small angle scattering, absorption and reactivity: A continuous flow catalysis reactor, *Nucl. Instruments Methods Phys. Res. Sect. A Accel. Spectrometers, Detect. Assoc. Equip.* 649 (2011) 200–203, <https://doi.org/10.1016/j.nima.2010.12.172>.
- [30] C. Trinh, Y. Wei, A. Yadav, M. Muske, N. Grimm, Z. Li, L. Thum, D. Wallacher, R. Schlögl, K. Skorupska, R. Schlattmann, D. Amkreutz, Reactor design for thin film catalyst activity characterization, *Chem. Eng. J.* 477 (2023) 146926, <https://doi.org/10.1016/j.cej.2023.146926>.
- [31] O.-S. Joo, K.-D. Jung, I. Moon, A.Y. Rozovskii, G.I. Lin, S.-H. Han, S.-J. Uhm, Carbon Dioxide Hydrogenation To Form Methanol via a Reverse-Water-Gas-Shift Reaction (the CAMERE Process), *Ind. Eng. Chem. Res.* 38 (1999) 1808–1812, <https://doi.org/10.1021/ie9806848>.
- [32] G. Centi, E.A. Quadrelli, S. Perathoner, Catalysis for CO<sub>2</sub> conversion: a key technology for rapid introduction of renewable energy in the value chain of chemical industries, *Energy Environ. Sci.* 6 (2013) 1711–1731, <https://doi.org/10.1039/C3EE00056G>.
- [33] E. Nowicka, S.M. Althahban, Y. Luo, R. Kriegel, G. Shaw, D.J. Morgan, Q. He, M. Watanabe, M. Armbrüster, C.J. Kiely, G.J. Hutchings, Highly selective Pd/ZnO catalysts for the methanol steam reforming reaction, *Catal. Sci. Technol.* 8 (2018) 5848–5857, <https://doi.org/10.1039/c8cy01100a>.
- [34] P. Kast, M. Friedrich, F. Girsdis, J. Kröhner, D. Teschner, T. Lunkenbein, M. Behrens, R. Schlögl, Strong metal-support interaction and alloying in Pd/ZnO catalysts for CO oxidation, *Catal. Today*. 260 (2016) 21–31, <https://doi.org/10.1016/j.cattod.2015.05.021>.
- [35] E. Nowicka, S. Althahban, T.D. Leah, G. Shaw, D. Morgan, C.J. Kiely, A. Roldan, G. J. Hutchings, Benzyl alcohol oxidation with Pd-Zn/TiO<sub>2</sub>: computational and experimental studies, *Sci. Technol. Adv. Mater.* 20 (2019) 367–378, <https://doi.org/10.1080/14686996.2019.1598237>.
- [36] H. Bahruji, M. Bowker, G. Hutchings, N. Dimitratos, P. Wells, E. Gibson, W. Jones, C. Brookes, D. Morgan, G. Lalev, Pd/ZnO catalysts for direct CO<sub>2</sub> hydrogenation to methanol, *J. Catal.* 343 (2016) 133–146, <https://doi.org/10.1016/j.jcat.2016.03.017>.
- [37] M. Zabilskiy, V.L. Sushkevich, M.A. Newton, F. Krumeich, M. Nachtegaal, J.A. van Bokhoven, Mechanistic study of carbon dioxide hydrogenation over Pd/ZnO-based catalysts: the role of palladium–zinc alloy in selective methanol synthesis, *Angew. Chemie - Int. Ed.* 60 (2021) 17053–17059, <https://doi.org/10.1002/anie.202103087>.
- [38] M. Bowker, N. Lawes, I. Gow, J. Hayward, J.R. Esquius, N. Richards, L.R. Smith, T. J.A. Slater, T.E. Davies, N.F. Dummer, L. Kabalan, A. Logsdail, R.C. Catlow, S. Taylor, G.J. Hutchings, The critical role of  $\beta\text{PdZn}$  alloy in Pd/ZnO catalysts for the hydrogenation of carbon dioxide to methanol, *ACS Catal.* 12 (2022) 5371–5379, <https://doi.org/10.1021/acscatal.2c00552>.
- [39] N. Lawes, K.J. Aggett, L.R. Smith, T.J.A. Slater, M. Dearn, D.J. Morgan, N. F. Dummer, S.H. Taylor, G.J. Hutchings, M. Bowker, Zn Loading Effects on the Selectivity of PdZn Catalysts for CO<sub>2</sub> Hydrogenation to Methanol, *Catal. Letters*. 154 (2024) 1603–1610, <https://doi.org/10.1007/s10562-023-04437-5>.
- [40] C. Quilis, N. Mota, B. Pawelec, E. Millán, R.M. Navarro Yerga, Intermetallic PdZn/TiO<sub>2</sub> catalysts for methanol production from CO<sub>2</sub> hydrogenation: The effect of ZnO loading on PdZn-ZnO sites and its influence on activity, *Appl. Catal. B Environ.* 321 (2023) 122064, <https://doi.org/10.1016/j.apcatb.2022.122064>.
- [41] O.A. Ojelade, S.F. Zaman, M.A. Daous, A.A. Al-Zahrani, A.S. Malik, H. Driss, G. Shterk, J. Gascon, Optimizing Pd:Zn molar ratio in PdZn/CeO<sub>2</sub> for CO<sub>2</sub> hydrogenation to methanol, *Appl. Catal. A Gen.* 584 (2019) 117185, <https://doi.org/10.1016/j.apcata.2019.117185>.
- [42] P. Ferrari, J. Vanbuel, Y. Li, T.-W. Liao, E. Janssens, P. Lievens, The Double-Laser Ablation Source Approach, in: *Gas-Phase Synth. Nanoparticles*, Wiley, 2017: pp. 59–78. 10.1002/9783527698417.ch4.
- [43] N. Binsted, J. Campbell, S.J. Gurman, P.C. Stephenson, *EXAFS analysis Programs; Daresbury Laboratory, Warrington, UK*, 1991.
- [44] COMSOL Multiphysics® v. 6.2. www.comsol.com. COMSOL AB, Stockholm, Sweden, (n.d.).
- [45] R.S. Brokaw, Predicting Transport Properties of Dilute Gases, *Ind. Eng. Chem. Process Des. Dev.* 8 (1969) 240–253, <https://doi.org/10.1021/1260030a015>.
- [46] J.A. Hernandez Lalinde, P. Roongruangsree, J. Ilsemann, M. Bäumer, J. Kopyscinski, CO<sub>2</sub> methanation and reverse water gas shift reaction. Kinetic study based on in situ spatially-resolved measurements, *Chem. Eng. J.* 390 (2020) 124629, <https://doi.org/10.1016/j.cej.2020.124629>.
- [47] M.J.L. Ginés, A.J. Marchi, C.R. Apesteguía, Kinetic study of the reverse water-gas shift reaction over CuO/ZnO/Al<sub>2</sub>O<sub>3</sub> catalysts, *Appl. Catal. A Gen.* 154 (1997) 155–171, [https://doi.org/10.1016/S0926-860X\(96\)00369-9](https://doi.org/10.1016/S0926-860X(96)00369-9).
- [48] A. Desagnés, I. Ililita, M.C. Ililita, Sorption-enhanced intensified CO<sub>2</sub> hydrogenation via reverse water-gas shift reaction: Kinetics and modelling, *Chem. Eng. J.* 494 (2024) 152052, <https://doi.org/10.1016/j.cej.2024.152052>.
- [49] J.E. Scheerder, T. Picot, N. Reckinger, T. Sneyder, V.S. Zharinov, J.F. Colomer, E. Janssens, J. Van De Vondel, Decorating graphene with size-selected few-atom clusters: A novel approach to investigate graphene-adparticle interactions, *Nanoscale*. 9 (2017) 10494–10501, <https://doi.org/10.1039/c7nr02217d>.
- [50] N. Vandamme, E. Janssens, F. Vanhoutte, P. Lievens, C. Van Haesendonck, Scanning probe microscopy investigation of gold clusters deposited on atomically flat substrates, *J. Phys. Condens. Matter.* 15 (2003) S2983–S2999, <https://doi.org/10.1088/0953-8984/15/42/001>.
- [51] E.C. Tyo, S. Vajda, Catalysis by clusters with precise numbers of atoms, *Nat. Nanotechnol.* 10 (2015) 577–588, <https://doi.org/10.1038/NNANO.2015.140>.
- [52] L. Chen, S.I. Allec, M.T. Nguyen, L. Kovarik, A.S. Hoffman, J. Hong, D. Meira, H. Shi, S.R. Bare, V.A. Glezakou, R. Rousseau, J. Szanyi, Dynamic Evolution of Palladium Single Atoms on Anatase Titania Support Determines the Reverse Water-Gas Shift Activity, *J. Am. Chem. Soc.* 145 (2023) 10847–10860, <https://doi.org/10.1021/jacs.3c02326>.
- [53] S.S. Kim, H.H. Lee, S.C. Hong, A study on the effect of support's reducibility on the reverse water-gas shift reaction over Pt catalysts, *Appl. Catal. A Gen.* 423–424 (2012) 100–107, <https://doi.org/10.1016/j.apcata.2012.02.021>.
- [54] A.A. Phatak, N. Koryakina, S. Rai, J.L. Ratts, W. Ruettinger, R.J. Farrauto, G. E. Blau, W.N. Delgass, F.H. Ribeiro, Kinetics of the water-gas shift reaction on Pt catalysts supported on alumina and ceria, *Catal. Today*. 123 (2007) 224–234, <https://doi.org/10.1016/j.cattod.2007.02.031>.
- [55] J.C. Van Giezen, F.R. Van Den Berg, J.L. Kleinen, A.J. Van Dillen, J.W. Geus, The effect of water on the activity of supported palladium catalysts in the catalytic combustion of methane, *Catal. Today*. 47 (1999) 287–293, [https://doi.org/10.1016/S0920-5861\(98\)00309-5](https://doi.org/10.1016/S0920-5861(98)00309-5).
- [56] D. Ciuparu, N. Katsikis, L. Pfefferle, Temperature and time dependence of the water inhibition effect on supported palladium catalyst for methane combustion, *Appl. Catal. A Gen.* 216 (2001) 209–215, [https://doi.org/10.1016/S0926-860X\(01\)00558-0](https://doi.org/10.1016/S0926-860X(01)00558-0).
- [57] C.Y. Lee, C.R. Wilke, Measurements of Vapor Diffusion Coefficient, *Ind. Eng. Chem.* 46 (1954) 2381–2387, <https://doi.org/10.1021/ie50539a046>.
- [58] F. Mayinger, *Transport Phenomena in Micro Process Engineering*, Springer Berlin Heidelberg, Berlin, Heidelberg, 2007. 10.1007/978-3-540-74618-8\_5.
- [59] J.R.H. Ross, *Contemporary Catalysis*, Elsevier (2019), <https://doi.org/10.1016/C2014-0-00159-1>.